RSC Advances

Synthesis of a novel and stable reduced graphene oxide/MOF hybrid nanocomposites and photocatalytic performance for the degradation of dyes

SCHOLARONE™
Manuscripts

1 **Synthesis of a novel and stable reduced graphene**

2 **oxide/MOF hybrid nanocomposites and photocatalytic**

3 **performance for the degradation of dyes**

4

5 Lizhang Huang,[a,b] Bingsi Liu[a*]

6

7 *[a]Department of Chemistry, Tianjin university, and Collaborative Innovation Center of*

8 *Chemical Science and Engineering (Tianjin), Tianjin 300072, People's Republic of*

9 *China*

10 *[b]Zhangzhou Product Quality Supervision and Inspection Institute (Zhangzhou),*

11 *Fujian 363000, People's Republic of China*

12

13

14

15

16

17

18

19

20

21

22

23

24

25

26

27

28

29   **Abstract:** a simple and facile solvothermal method is developed for the preparation of

30   reduced graphene oxide/NH$_2$-MIL-125(Ti) (rGO-NMTi) hybrid nanocomposite

31   photocatalysts with large specific surface area and thermal stability. This

32   rGO-NMTi-x hybrid nanocomposite exhibited more efficient photocatalytic

33   performance than NH$_2$-MIL-125(Ti) for methyl blue (MB) degradation under

34   visible-light irradiation due to the synergetic action between rGO and

35   NH$_2$-MIL-125(Ti). Therefore, rGO/MOFs photocatalysts have great potentiality in

36   environmental remediation. The structure and physical properties of rGO,

37   NH$_2$-MIL-125(Ti) and rGO-NMTi-x hybrid nanocomposites were characterized by

38   means of scanning electron microscopy (SEM), X-ray diffraction (XRD), N$_2$

39   adsorption/desorption, high resolution transmission electron microscope (HRTEM),

40   laser Raman, UV-visible absorption spectra (UV-DRS) and FT-IR techniques.

43

44

45

46

47

48

49

50

51

52

53

1. Introduction

As an environmentally friendly and cost-effective technology, visible light driven photocatalysis for removal of organic pollutant has been extensively studied.[1-3] The photocatalytic activity of the photocatalysts with nanostructure depends strongly on their composition and structure.[4-6] The main serious obstacles in developing hybrid photocatalysts are including poor affinity between pollutants and photocatalyst,[7] rapid recombination of photogenerated electron-hole pairs,[8] low-light-harvesting efficiency of photocatalyst,[9] and short light residence time on/in the photocatalysts.[10,11] Metal-organic frameworks (MOFs), a novel class of hybrid materials constructed by metal-containing nodes connected by organic bridges, have attracted a great deal of attention due to their useful applications in gas storage, separation, catalysis, sensors, and other technologies.[12-15] However, the performance of MOFs served as catalysts in photocatalysis is not comparable to that of inorganic semiconductors due to the low efficiency for solar energy conversion and photo-generated charge separation.

Hybrid material, a novel mixture of material has attracted a great deal of attention due to the exciting properties compared with pure counterparts.[16,17] Compared with pure MOFs, the hybrids integrating MOFs with inorganic species (CdS, TiO_2, Fe_3O_4, Cu_2O, Au, Pd, and Pt) acted as photocatalysts presented significant advantages than the pure MOFs, owing to their synergism effect.[18-24] He *et al.* reported that the photocatalytic hydrogen production efficiency of CdS-MIL-101 hybrid materials under visible-light irradiation was superior to pure CdS nano-particles owing to photocatalytic reaction centers with high visible light harvesting capability, more active adsorption sites, and

76   high specific surface area.[18] Thus, far much attention has been focused on

77   carbon-based materials, which contains a lot of prospective materials such as,

78   graphene quantum dots (QDs),[25] graphene,[26,27] fullerene,[28] and carbon nanotubes.[29]

79   All of them are extensively used as catalyst owing to their large specific surface area,

80   excellent mechanical and hydrophobic properties as well as chemically stability. In

81   addition, graphene exhibits several photocatalyst properties,[30-35] including the

82   extension of the duration of electron-hole pair, the enhancement of light adsorption

83   range and intensity. According to the report of Qiu et $al,$[36] TiO_2/graphene composites

84   with high electrical conductivity and three-dimensional hierarchically porous structure

85   prepared by one-step method exhibits potential photoactivity. Gan et al [37] studied the

86   P25/graphene composite in degrading aquatic organic pollutants and discussed the

87   contribution of photothermal effect in the photocatalytic performance.[38] Zhang et al

88   and Wu et al[39-41] reported the MIL-88(Fe)@GO and the GR/MIL-53(Fe)-H_2O_2

89   photocatalytic materials, respectively for the degradation of dye or Rhodamine B.

90   However, NH_2-MIL-125(Ti), as a highly porous MOFs photochemical property, not

91   only contained high density of the immobilized Ti sites, but also presented

92   isostructural MOFs with improved photocatalytic properties by tuning the

93   incorporation of organic ligands. Therefore，the reduced graphene oxide/NH_2-MIL-

94   125(Ti) (rGO-NMTi) hybrid materials were designed and synthesized by a simple and

95   facile solvothermal method. Its photocatalytic activity towards methyl blue (MB) dye

96   degradation under visible-light irradiation was evaluated. The photocatalytic

97   mechanism as well as the reusability and stability of photocatalyst, an

98   environmental-friendly optimizing hybrid nanocomposite were investigated. The

99   structure and physical properties of hybrid nanocomposite photocatalysts were

100   characterized by means of SEM, HRTEM，Laser Raman, XRD, FT-IR, N_2

101   adsorption–desorption, and UV–vis DRS techniques.

2. Experimental

2.1. Materials

104   Sodium nitrate, hydrochloric acid, hydrogen peroxide (30%), barium chloride,

105   sulfuric acid and potassium permanganate were purchased from Shantou Xilong

106   chemical Co., Ltd, China. Graphite powder was received from Sinopharm Chemical

107   Regent. 2-amino-benzene-1,4-dicarboxylate (NH_2-BDC) and tetra-n-butyl titanate

108   $Ti(OC_4H_9)_4$ (TPOT) were purchased from Alfa Aesar Co., Ltd, China and Shanghai

109   Chemical Reagent Co., Ltd, China, respectively. These reagents were analytical grade

110   and used without further purifications.

2.2 Synthesis of GO and rGO/NH_2-MIL-125(Ti) hybrid materials

112   Graphite oxide (GO) was prepared according to the methods in literature.[42] The

113   NH_2-MIL-125(Ti) was synthesized according to the previously reported method with

114   slight modification.[43] A certain amount of GO powder was dispersed into methanol

115   with the aid of ultrasonication. Then, TPOP (2.3 mL), NH_2-BDC (2.1 g), DMF (35

116   mL), and GO-methanol (4.0 mL) mixture was subjected to solvothermal conditions in

117   a Teflon-lined stainless-steel autoclave. The resulting solution was treated by

118   ultrasonic for 15 min to obtain a uniformly dissolution of the reactants, and then kept

119   at 120 $^{\rm o}$C for 48 h. After reaction, the resultant precipitate was separated by

120   centrifugation, washed repeatedly with DMF and methanol, respectively. Finally, the

121   as-obtained hybrid materials were dried at 100 $^{\circ}$C under vacuum for 24 h. As-obtained

122   precipitant were denoted as rGO-NMTi-1, rGO-NMTi-2, rGO-NMTi-3, and

123   rGO-NMTi-4, where 1, 2, 3 and 4 represent the 5, 10, 15 and 20 wt% of GO in the

124   samples, respectively. For comparison purposes, the conventional NH_2-MIL-125(Ti)

125   was prepared in the absence of GO under the same conditions.

126   **2.3 Characterization**

127   Morphology of the samples was characterized by a scanning electron microscopy

128   (SEM) on a Gemini microscope (Hitachi, S-4800, Japan) at an accelerating voltage of

129   10 kV. X-ray diffraction (XRD) patterns were collected on a Panaltical X'Pert-pro

130   MPD X-ray power diffractometer (Cu Kα irradiation source, λ = 1.54056 Å).

131   UV-visible absorption spectra (UV-DRS) of the hybrid nanocomposites were

132   obtained for the dry-pressed disk samples using a Cary 500 Scan Spectrophotometer

133   (Varian, USA). The IR experiments were carried out on a Nicolet 670 FT-IR

134   spectrometer in the range of 4000-400 cm^{-1}. Transmission electron microscope (TEM)

135   was conducted on FEI Tecnai G2 S-TWIN and the accelerating voltage was 200 kV.

136   Raman spectroscopy was measured on Renishaw inVia plus using 633 nm laser

137   excitation (Microplate reader: Biocell HT2). Brunauer-Emmett-Teller (BET) surface

138   area of the samples was measured using a sorptometer (ASAP-2420, Micromeritics,

139   USA) at 77 K.

140   **2.4 Photocatalytic evaluation**

141   Photocatalytic degradation of methyl blue (MB) was carried out in a 100 mL beaker

142   containing 40 mL of methyl blue solution (5.4×10^{-5} mol/L) and photocatalyst (30 mg).

143   The solution was stirred magnetically in a dark room for 20 min to get

144   adsorption–desorption equilibrium. The solution was then irradiated under

145   visible-light illumination (> 420 nm). A 300 W Xenon lamp (Beijing China Education

146   Au-light, Co. Ltd.) with a 420 nm cutoff filter was used as the visible-light source. At

147   certain time intervals, 4 mL of aliquots were sampled and centrifuged to remove the

148   photocatalyst. The MB concentration was determined using a UV–vis

149   spectrophotometer at the wavelength of 663 nm. The degradation rate was calculated

150   using below equation.

151   Degradation rate = $(C_0\text{-}C) \times 100\%$ /C_0

152   C_0 and C are the MB concentrations before and after visible light photodegradation,

153   respectively.

3. Results and discussion

3.1. Morphology and structure of rGO-NMTi-x hybrid materials

156   The morphologies of rGO-NMTi-x were clearly observed by scanning electron

157   microscopy (SEM), and SEM images of GO and NH_2-MIL-125(Ti) are also shown in

158   Fig. 1 for comparison. It can be seen that the GO presented a sheet structure with

159   wrinkle (Fig. 1a) whereas the morphology of NH_2-MIL-125(Ti) (Fig. 1b) looks like

160   the snowflake or cotton with some traces of amorphous phase. After a certain amount

161   of GO powder was introduced during the synthesis, the SEM image of rGO-NMTi-x

162   (Fig. 1c-f) revealed that the particles of NH_2-MIL-125(Ti) agglomerated slight with

163   different surface morphology. Moreover, the agglomerates of rGO-NMTi-1

164   nanocomposite look different from pure NH_2-MIL-125(Ti). The sandwich-like

165   structure between NH_2-MIL-125(Ti) and rGO is not clearly in rGO-NMTi-1 due to

166   low resolution. It is very possible that the introduction of more GO interfere with the

167   NH_2-MIL-125(Ti) crystal, which are even more visible for rGO-NMTi-3 (with 15

168   wt% GO) and the particles of NH_2-MIL-125(Ti) become larger with incremental GO

169   loadings (Fig. 1f).

170

171   **Fig. 1.**

172   The powder XRD patterns of rGO, NH_2-MIL-125 (Ti) and rGO-NMTi-x are

173   shown in Fig. 2, it can be seen that there is a broad peak at $2\theta = 26^o$, a typical

174   character of amorphous carbon or graphene for rGO sample. In the meantime, the

175   NH_2-MIL-125(Ti) presented a typical structure of inorganic crystal (Fig. 2b), which

176   are consistent with the result reported previously,[43] demonstrating that preparation of

177   rGO and NH_2-MIL-125(Ti) are successful. Interestingly, for the hybrid composites,

178   rGO-NMTi-x, a broad peak at $2\theta = 26^o$ reduced slightly compared to that of rGO but

179   these peaks intensified with an increasing GO content (Fig. 2c-f), indicated that the

180   amorphous structure of rGO existed in rGO-NMTi-x samples. According to the report

181   of Hafizovic *et al*,[44] the presence of carboxylic groups on the surface of rGO would

182   result in a distortion of the cubic symmetry. Hence, the characteristic peaks of

183   NH_2-MIL-125(Ti)   reduced   or/and   disappeared   in   the   rGO-NMTi-x   hybrid

184   nanocomposites (Fig. 2c-f) due to the differences in the building units of

185   rGO-NMTi-2 and the other hybrid nano-composites. It is well known that the

186   structure of both GO and NH_2-BDC is π-rich, there should be strong π-π interactions

187   between them. Therefore, the presence of GO sheets may unusually bend the

188   NH_2-BDC linker and results in severe twisting of the $TiO_5(OH)$ paddle wheel from an

189   ideal octahedral square grid. Due to this distortion, the NH_2-MIL-125(Ti) crystals

190   would exist in a body centered unit cell instead of a primitive cell with symmetry.[45,46]

191   Therefore, the introduction of GO can affect the crystallization of NH_2-MIL-125(Ti)

192   and control the morphology of such heterostructures.

193

194   **Fig. 2.**

195

196   **3.2 FT-IR spectra, UV–vis DRS and specific surface area of the hybrid materials**

197   Figure 3 showed the FT-IR spectra of rGO, NH_2-MIL-125(Ti) and rGO-NMTi

198   hybrid nanocomposites in the range of 500–4000 cm^{-1}. It can be seen that a broad

199   peak at 3400 cm^{-1} can be attributed to the O–H vibration of H_2O in the FT-IR

200   spectrum of GO. The absorption bands of C=O and C-O were observed at 1718 and

201   1250 cm^{-1} in the spectrum of NH_2-MIL-125(Ti) and rGO-NMTi-x hybrid

202   nanocomposites. Moreover, NH_2-MIL-125(Ti) and rGO-NMTi-x hybrid nano-

203   composites present characteristic bands of the carboxylate in 1380-1600 cm^{-1} as well

204   as the vibrations of O-Ti-O groups at 400-800 cm^{-1}. These results verified further that

205   the solvothermal synthesis of rGO-NMTi-x hybrid nanocomposites still maintained

206   intact MOF structure of NH_2-MIL-125(Ti).

207

208   **Fig. 3.**

209

210 The UV–vis DRS analysis of rGO-NMTi-x hybrid nanocomposites was conducted on

211 a Cary 500 scan spectrophotometer. As shown in Fig. 4，a notable absorption

212 extension in the visible-light region can be observed for rGO-NMTi-x hybrid

213 nanocomposites and the optical absorption intensity enhances with the increase of

214 rGO contents. According to the report of Fu *et al*,[43] there was absorption peak at 250

215 nm with absorption edge to 350 nm for MIL-125(Ti) whereas NH_2-MIL-125(Ti)

216 showed an extra absorption band at 400 nm with the absorption edge extending to ca.

217 550 nm, which originated from the induction effect of an amino functionality for its

218 optical absorption, in agreement with our observation (Fig.4 a-b). However, it is of

219 interest to note that a notable absorption extension band is observed (Fig.4c-d) in the

220 visible-light region when the content of rGO was more than or equal to 15% in

221 rGO-NMTi-x hybrid nanocomposites. According to Zhang *et al*[41] for GR/MIL-53(Fe)

222 composites, the optical absorption intensity in the range 500−800 nm increased

223 remarkably after combination with appropriate amount of GR, which attributed to the

224 background absorption of GR. We considered that the GO underwent quick

225 deoxygenation (removal of epoxide and hydroxyl functional groups), which reflected

226 enhanced π-electron conjugation and structural ordering with the restoration of sp^2

227 carbon and possible rearrangement of atoms. FT-IR of rGO-NMTi-x (Fig. 3d and 3e)

228 also confirmed that the vibration spectra of C=O changed obviously which correlated

229 closely with energy band gap structure[47]. In the meantime, the change in color is

230 companied form dark green of rGO-NMTi-2 to grey black of rGO-NMTi-3 (inset in

231 Fig. 4.), in agreement with previous observations in other rGO based composites.[41] It

232   indicated that the synergetic action between rGO and NH_2-MIL-125(Ti) can reduce

233   successfully the recombination rate of the electron–hole pair in the rGO-NMTi hybrid

234   nanocomposites. The red shift of absorption wavelength suggested that these

235   nanocomposites can absorb effectively visible-light for the application in the

236   visible-light photocatalysis.[48]

237

238   **Fig. 4.**

239   To further identify structural properties of the rGO-NMTi composites, Fig. 5a and

240   5b illustrated HRTEM images of rGO-NMTi-3; it can be seen that the irregular ball

241   nanoparticles of NH_2-MIL-125(Ti) are embedded in the wrinkling rGO lamellar

242   structure and its morphology is similar to the observation from SEM of samples (Fig.1)

243   which is different entirely from the rod-shaped structure of MIL-88(Fe)@GO reported

244   in literature[39-40]. In addition, there were two typical peaks, G at 1595 cm^{-1} and D at

245   1325 cm^{-1} in Raman spectrum of rGO-NMTi-3 composite (Fig. 5c), meaning the

246   existence of rGO in rGO-NMTi-3. According to the report of Li et al,[49] The G peak is

247   associated with the first-order scattering of E_{2g} mode for sp^2 hybridized carbon

248   domain and the D peaks are assigned to the structural defects corresponding to

249   sp^3 hybridization. Furthermore, the ratio of I_D and I_G was 1.05, indicating the efficient

250   reduction of GO during solvothermal process. The abroad peaks appeared at about

251   1063, 856, 652, and 463 cm^{-1} are corresponding to the characteristic vibrations of

252   metal terephthalate (Fig. 5c), similar to the observation in MIL-53(Fe)[H_2O].[40]

253   As shown in Fig. 5d, the N_2 adsorption/desorption isotherms observed over

254   rGO-NMTi-3 and NH$_2$-MIL-125(Ti) attributed to IV-type adsorption curve. It can be

255   seen that the adsorption contents at pressure range of p/p_0 = 0.05-0.3 increased

256   remarkably, meaning the existence of a large amount of micropores in

257   NH$_2$-MIL-125(Ti) whereas when the pressure range of p/p_0 is more than 0.4, both

258   adsorption capacities almost kept at a constant. The shape of hysteresis loop between

259   adsorption and desorption branches illustrated the existence of slit-pores in the

260   rGO-NMTi-3, which consisted of micro- and meso-pore. The specific surface areas of

261   rGO-NMTi-3 and NH$_2$-MIL-125(Ti), calculated *via* Brunauer-Emmett-Teller (BET)

262   method are 750.3 and 1233 m^2 g^{-1}, respectively.

263

264   **Fig. 5.**

265

266   **3.3 Photocatalytic performance of rGO-NMTi-x**

267   The photocatalytic activities of the as-synthesized NH$_2$-MIL-125(Ti) and

268   rGO-NMTi-x hybrid nano-composites were evaluated *via* the photodegradation of

269   MB under visible light irradiation (> 420 nm), as shown in Fig. 6. It can be seen that

270   there is not the photodegradation of MB to occur in the absence of photocatalyst

271   (Fig.6a) whereas all of rGO-NMTi-x photocatalysts show much higher photocatalytic

272   activities than NH$_2$-MIL-125(Ti) for the photodegradation of MB under the same

273   experimental conditions due to the synergistic effect between NH$_2$-MIL-125(Ti) and

274   rGO. However, when the rGO content increased to 20 wt% there was a slight decrease

275   in photocatalytic activity (Fig. 6e), which is still better photocatalytic performance of

276   NH$_2$-MIL-125(Ti) due to the fact that the higher contents of rGO in the rGO-NMTi-x

277   hybrid nanocomposites will result in an redundant ratio between rGO and

278   NH_2-MIL-125(Ti), thereby lowering the electron transfer efficiency of the

279   photoinduced electrons on NH_2-MIL-125(Ti) to rGO surfaces. We may envisage that

280   the photocatalytic activity of rGO-NMTi-4 declines with much higher loading in the

281   composite photocatalyst under visible light irradiation. This result indicates that both

282   rGO and NH_2-MIL-125(Ti) play an important role in improving the photocatalytic

283   activity due to the significant synergistic effect between rGO and NH_2-MIL-125(Ti)

284   for the photodegradation of MB under visible light irradiation.

285

286   **Fig. 6.**

287

288   **3.4. Clarification of the reaction mechanism.**

289   It is well known that high adsorption ability, an efficient charge migration, and

290   large surface area play a vital role for improving the photocatalytic activity.[50] The

291   existence of rGO sheets could facilitate charge migration and reduce the

292   recombination of electron–hole pairs of the rGO based photocatalysts.[51] Here, a

293   possible photocatalytic process is schematized in Fig. 7. The photo-generated

294   electrons originated from MB or rGO transfer to the Ti^{4+} in the titanium–oxo clusters

295   of NH_2-MIL-125(Ti) due to the adsorption or the heterojunction structure, Ti^{4+} is thus

296   reduced to Ti^{3+}. Oxygen molecules adsorbed onto porous NH_2-MIL-125(Ti) to form

297   superoxide ($\cdot O^{2-}$) ion radicals *via* electron transfer from Ti^{3+} to O_2 molecules due to

298   the strong reducing ability of Ti^{3+}. The Ti^{3+} ions are oxidized and further convert to

299   Ti^{4+} ions. The electron transportation in the titanium–oxo clusters of NH_2-MIL-125(Ti)

300   *via* the presence of Ti^{3+}–Ti^{4+} intervalence electron transfer had been verified by

301   previous reports.[43] The formed •O^{2-} radicals could efficiently degrade MB (or MB^+•)

302   into CO_2 and water. Simultaneously, the generated holes of rGO are capable of

303   oxidizing MB directly.[52]

304

305   **Fig. 7.**

306

307   **3.5. Recyclability and stability of rGO-NMTi-3**

308   The recycle experiments of rGO-NMTi-3 for photocatalytic reaction were carried

309   out under the condition of visible-light irradiation to evaluate the stability of the

310   photocatalyst. As shown in Fig. 8a, the efficiency for the photodegradation of MB

311   after 5th-runs are still kept above 96.7%, indicating that the rGO-NMTi-3 can be used

312   successively without the variation of photocatalytic performance during the oxidation

313   of pollutant. The HRTEM images, XRD and Raman results of rGO-NMTi-3 before

314   and after 5th-runs (Fig. 5a-c and Fig. 8b-d) revealed the high stability of the

315   rGO-NMTi-3 photocatalyst in the structure and composition. Therefore, rGO-NMTi-3

316   hybrid nano-composites can be used as efficient visible-light photocatalyst for

317   application in wastewater treatment.

318   **Fig. 7.**

319

320   **4. Conclusion**

321   A series of rGO-NMTi-x hybrid nanocomposites with large surface area, high

322   activity and stability were successfully synthesized by means of a simple

323   solvothermal strategy where rGO acted as the support for the formation of

324   heterostructures. The results indicated that the rGO-NMTi-3 hybrid nanocomposites

325   showed remarkably higher photocatalytic performance for the degradation of MB than

326   NH_2-MIL-125(Ti) under the condition of visible-light irradiation due to the

327   synergistic effect between NH_2-MIL-125(Ti) and rGO as well as the Ti^{3+}–Ti^{4+}

328   intervalence electron transfer. Furthermore, the rGO-NMTi-3 hybrid nanocomposites

329   can be used as efficient visible-light photocatalyst for application in wastewater

330   treatment in the near future.

331

335

336   **References**

337   1 X. Xu, C. Randorn, P. Efstathiou and J. T. Irvine, *Nat. Mater.*, 2012, **11**, 595.

338   2 M. A. Shannon, P. W. Bohn, M. Elimelech, J. G. Georgiadis, B. J. Marinas and A.

339   M. Mayes, *Nature*, 2008, **452**, 301.

340   3 T. P. Yoon, M. A. Ischay and J. Du, *Nat. Chem.*, 2010, **2**, 527.

341   4 H. Zhang, X. Lv, Y. Li, Y. Wang and J. Li, *ACS Nano*, 2009, **4**, 380.

342   5 J. Zhang, Q. Xu, Z. Feng, M. Li and C. Li, *Angew. Chem. Int. Ed.*, 2008, **47**, 1766.

343   6 O. K. Varghese, M. Paulose, T. J. LaTempa and C. A. Grimes, *Nano Lett.*, 2009, **9**,

344   731.

345   7 H. Yu, S. Chen, X. Fan, X. Quan, H. Zhao, X. Li and Y. Zhang, *Angew. Chem. Int.*
346   *Ed.*, 2010, **49**, 5106.

347   8 R. Li, F. Zhang, D. Wang, J. Yang, M. Li, J. Zhu, X. Zhou, H. Han and C. Li, *Nat.*
348   *Commun.*, 2013, **4**, 1432.

349   9 F. Huang, D. Chen, X. L. Zhang, R. A. Caruso and Y. B. Cheng, *Adv. Funct. Mater.*,
350   2010, **20**, 1301.

351   10 S. Mubeen, J. Lee, N. Singh, S. Kramer, G.D. Stucky and M. Moskovits, *Nat.*
352   *Nanotechnol.*, 2013, **8**, 247.

353   11 W. Chen, Z. Fan, B. Zhang, G. Ma, K. Takanabe, X. Zhang and Z. Lai, *J. Am.*
354   *Chem. Soc.*, 2011, **133**, 14896.

355   12 L. J. Murray, M. Dinca and J. R. Long, *Chem. Soc. Rev.*, 2009, **38**, 1294.

356   13 J. R. Li, R. J. Kuppler and H. C. Zhou, *Chem. Soc. Rev.*, 2009, **38**, 1477.

357   14 J. Lee, O. K. Farha, J. Roberts, K. A. Scheidt, S. T. Nguyen and J. T. Hupp, *Chem.*
358   *Soc. Rev.*,2009, **38**, 1450.

359   15 A. C. McKinlay, R. E. Morris, P. Horcajada, G. Ferey, R. Gref, P. Couvreur and C.
360   Serre, Angew. Chem. Int. Ed., 2010, **49**, 6260.

361   16 G. Kickelbick, ed. *Hybrid materials*. 2007, Wiley-vch.

362   17 J. Su, M. Cao, L. Ren and C. Hu, *J. Phys. Chem. C*, 2011, **115**, 14469.

363   18 J. He, Z. Yan, J. Wang, J. Xie, L. Jiang, Y. Shi, F. Yuan, F. Yu and Y. Sun, *Chem.*
364   *Commun.*, 2013, **49**, 6761.

365   19 S. Abedi and A. Morsali, *ACS Catal.*, 2014, **4**, 1398.

366   20 C. F. Zhang, L. G. Qiu, F. Ke, Y. J. Zhu, Y. P. Yuan, G. S. Xu and X. Jiang, *J.*
367   *Mater. Chem. A*, 2013, **1**, 14329.

368   21 K. Jayaramulu, V. M. Suresh and T. K. Maji, *Dalton Trans.*, 2015, **44**, 83.

369   22 G. Lu, S. Z. Li, Z. Guo, O. K. Farha, B. G. Hauser, X. Y. Qi, Y. Wang, X. Wang,
370   S. Y. Han, X. G. Liu, J. S. DuChene, H. Zhang, Q. C. Zhang, X. D. Chen, J. Ma, S.
371   C. J. Loo, W. D. Wei, Y. H. Yang, J. T. Hupp and F. W. Huo, *Nat. Chem.*, 2012, **4**,
372   310.

373   23 W. N. Zhang, G. Lu, C. L. Cui, Y. Y. Liu, S. Z. Li, W. J. Yan, C. Xing, Y. R. Chi,
374   Y. H. Yang and F.W. Huo, *Adv. Mater.*, 2014, **26**, 4056.

375 24 A. Aijaz, A. Karkamkar, Y.J. Choi, N. Tsumori, E. Ronnebro, T. Autrey, H.

376   Shioyama and Q. Xu, *J. Am. Chem. Soc.*, 2012, **134**, 13926.

377 25 W. X. Zhang, J. Z. Zheng, C. H. Tan, X. Lin, S. R. Hu, J. H. Chen, X. L. You and

378   S. X. Li, *J. Mater. Chem. B*, 2015, **3**, 217.

379 26 S. H. Cheng, T. M. Weng, M. L. Lu, W. C. Tan, J. Y. Chen and Y. F. Chen, *Sci.*

380   *Rep.*, 2013, **3**, 2694.

381 27 L. L. Tan, W. J. Ong, S. P. Chai and A. R. Mohamed, *Nanoscale Res. Lett.*, 2013,

382   **8**,465.

383 28 Y. Y. Fan , W. G. Ma , D. X. Han ,   S. Y. Gan , X. D. Dong , and L. Niu, *Adv.*

384   *Mater.*, 2015, **27**, 3767.

385 29 R. Tenne, *Nat. Nano*, 2006, **1**, 103.

386 30 M. M. Gui, S. P. Chai, B. Q. Xu and A. R. Mohamed, *Sol. Energy Mater. Sol.*

387   *Cells*, 2014, **122**, 183.

388 31 H. Zhang, X. Lv, Y. Li, Y. Wang and J. Li, *ACS Nano*, 2010, **4**, 380.

389 32 J. Du, X. Y. Lai, N. L. Yang, J. Zhai, D. Kisailus, F. B. Su, D. Wang and L. Jiang,

390   *ACS Nano*, 2011, **5**, 590.

391 33 C. Liu, Y. Teng, R. Liu, S. Luo, Y. Tang, L. Chen and Q. Cai, *Carbon*, 2011, **49**,

392   5312.

393 34 O. Akhavan, M. Abdolahad, A. Esfandiar and M. Mohatashamifar, *J. Phys. Chem.*

394   *C*, 2010, **114**, 12955.

395 35 N. Li, G. Liu, C. Zhen, F. Li, L. L. Zhang and H. M. Cheng, *Adv. Funct.*

396   *Mater.*,2011, **21**, 1717.

397 36 N. Yang, J. Zhai, D. Wang, Y. Chen and L. Jiang, *ACS Nano*, 2010, **4**, 887.

398 37 B. C. Qiu, M. Y. Xing and J. L. Zhang, *J. Am. Chem. Soc.*, 2014, **136**, 5852.

399 38 Z. X. Gan, X. L. Wu, M. Meng, X. B. Zhu, L. Yang, and P. K. Chu, *ACS Nano*,

400   2014, **8**, 9304.

401 39 Y. Wu, H. Luo and H. Wang, *RSC Adv.*, 2014, **4**, 40435.

402 40 Y. Zhang, G. Li, H. Lu, Q. Lv and Z. Sun, *RSC Adv.*, 2014, **4**, 7594.

403 41 C. H. Zhang, L. H. Ai and J. Jiang, *Ind. Eng. Chem. Res.*, 2015, **54**, 153.

404 42 C. H. Tan, W. X. Zhang, J. Z. Zheng, X. L. You, X. Lin and S. X. Li, *J. Mater.*

405   *Chem. B*, 2015, **3**, 7117.

406 43 Y. H. Fu, D. R. Sun, Y. J. Chen, R. K. Huang, Z. X. Ding, X. Z. Fu and Z. H. Li,

407   *Angew. Chem. Int. Ed.*, 2012, **124**, 3420.

408 44 J. Hafizovic, M. Bjørgen, U. Olsbye, P. D. C. Dietzel, S. Bordiga, C. Prestipino, C.

409   Lamberti and K. P. Lillerud, *J. Am. Chem. Soc.*, 2007, **129**, 3612.

410 45 M. Dan-Hardi, C. Serre, T. Frot, L. Rozes, G. Maurin, C. Sanchez and G. Férey, *J.*

411   *Am. Chem. Soc.*, 2009, **131**, 10857.

412 46 M. Jahan, Z. Liu and K.P. Loh, *Adv. Funct. Mater.*, 2013, **23**, 5363.

413 47. B. R. Singh, M. Shoeb, W. Khan, A. H. Naqvi, *J. Alloys Comps,* 2015, **651,** 598.

414 48 J. He, Z. Yan, J. Wang, J. Xie, L. Jiang, Y. Shi, F. Yuan, F. Yu and Y. Sun, *Chem.*

415   *Commun.*, 2013, **49**, 6761.

416 49 S. X. Li, J. Z. Zheng, D. J. Chen, Y. j. Wu, W. X. Zhang, F. Y. Zheng, J. Cao and

417   Y. L. Liu, *Nanoscale*, 2013, **5**, 11718.

418 50 P. Wang, B. Huang, Y. Dai and M. H. Whangbo, *Phys. Chem. Chem. Phys.*, 2012,

419   **14**, 9813.

420 51 N. Zhang, M. Q. Yang, S.Q. Liu, Y. G Sun and Y. J. Xu, *Chem. Rev.*,2015, **115**,

421   10307.

422 52 L. Shi, L. Liang, J. Ma, F. Wang and J. Sun, *Catal. Sci. Technol.*, 2014, **4**, 758.

423

424
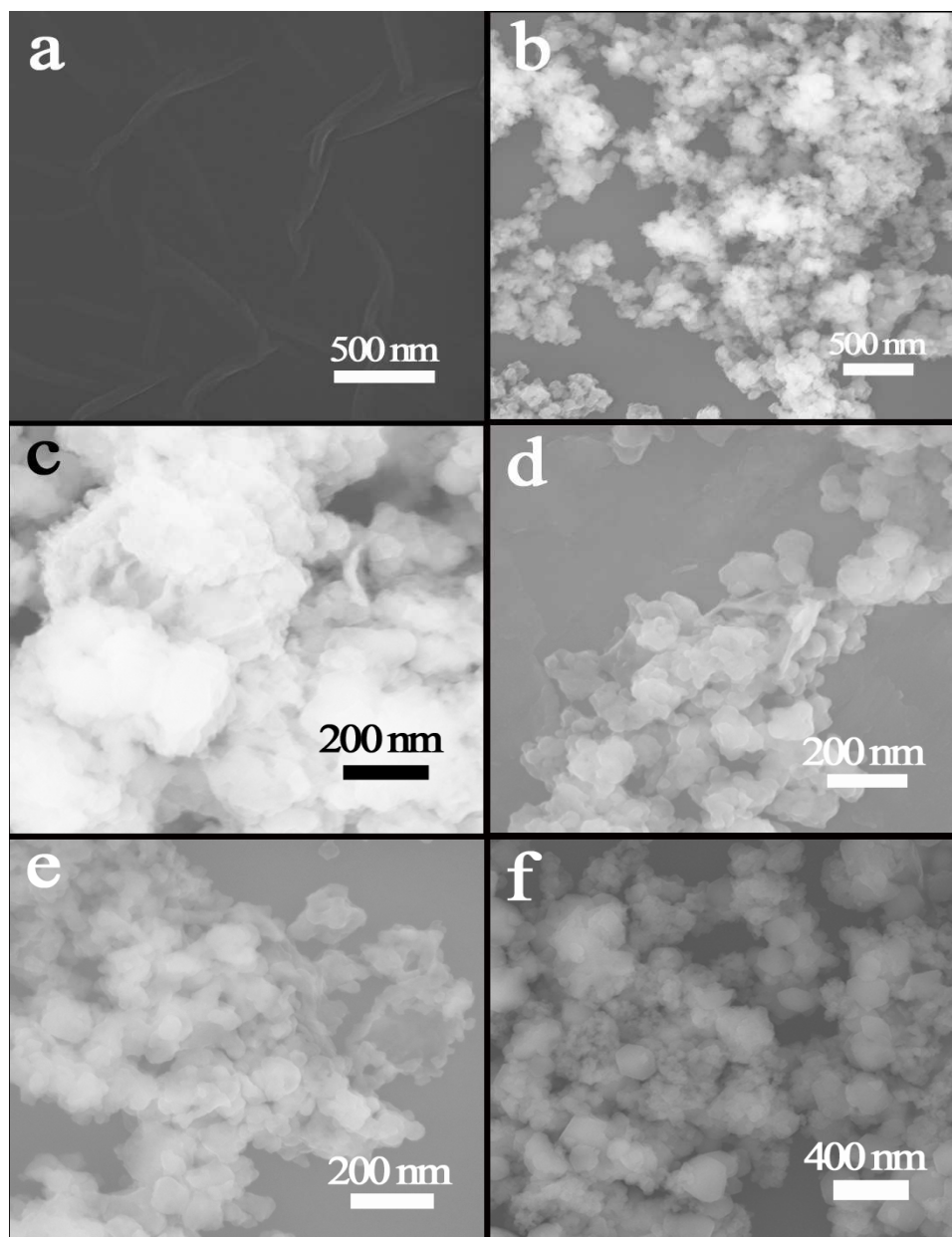
425

426

427

428

429

430

431

Figure captions

Fig. 1. SEM images for the parent materials and the hybrid nanocomposites. (a) GO, (b) NH_2-MIL-125(Ti), (c) rGO-NMTi-1, (d) rGO-NMTi-2, (e) rGO-NMTi-3, and (f) rGO-NMTi-4.
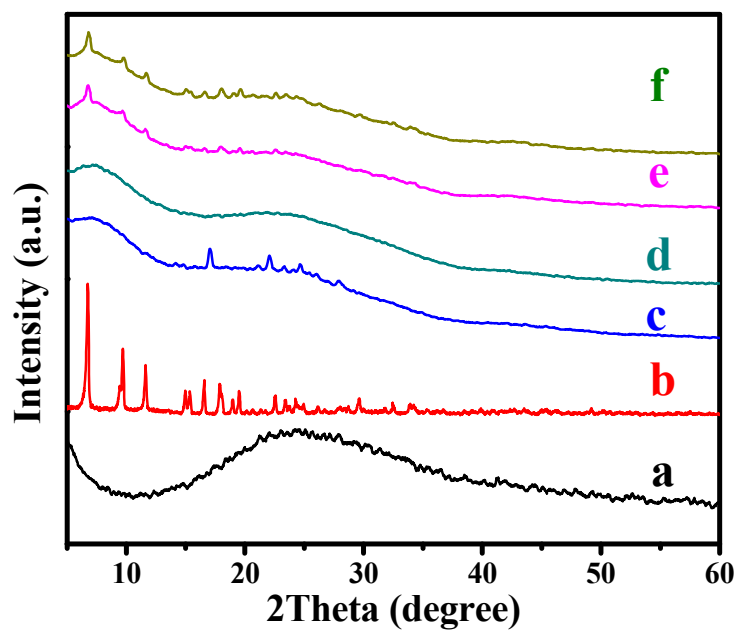
Fig. 2. XRD patterns of (a) rGO, (b) NH_2-MIL-125(Ti), (c) rGO-NMTi-1, (d) rGO-NMTi-2, (e) rGO-NMTi-3 and (f) rGO-NMTi-4 hybrid composite.
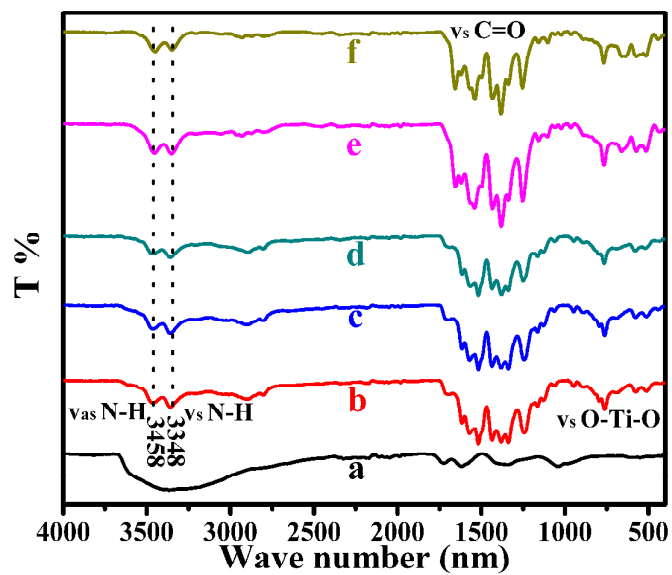
Fig. 3. FT-IR spectra of (a) GO, (b) NH_2-MIL-125(Ti), (c) rGO-NMTi-1, (d) rGO-NMTi-2, (e) rGO-NMTi-3, and (f) rGO-NMTi-4.
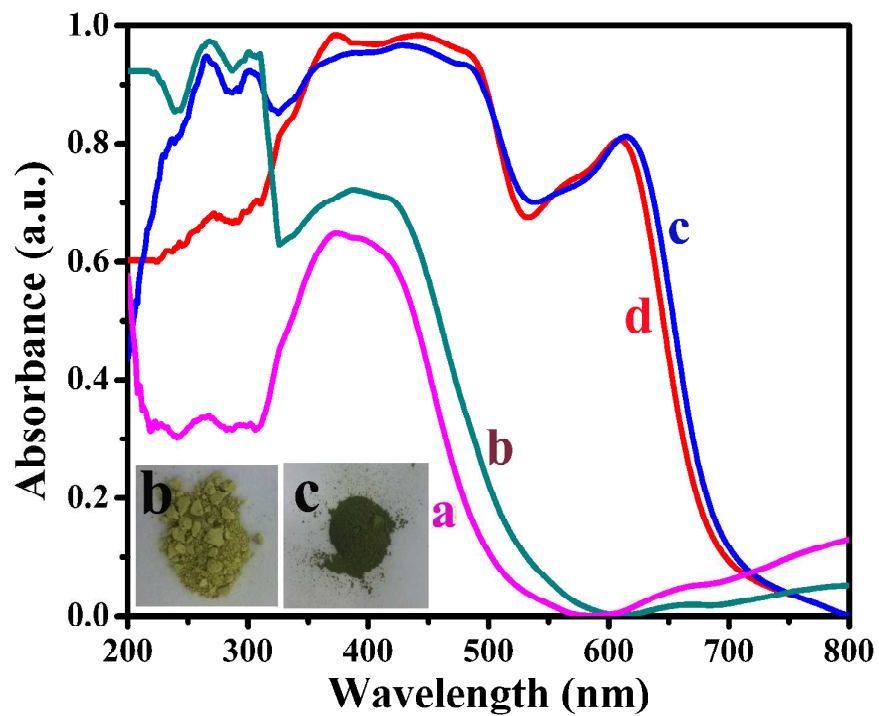
Fig. 4. UV–vis DRS spectrum of (a) rGO-NMTi-1, (b) rGO-NMTi-2, (c) rGO-NMTi-3, and (d) rGO-NMTi-4.
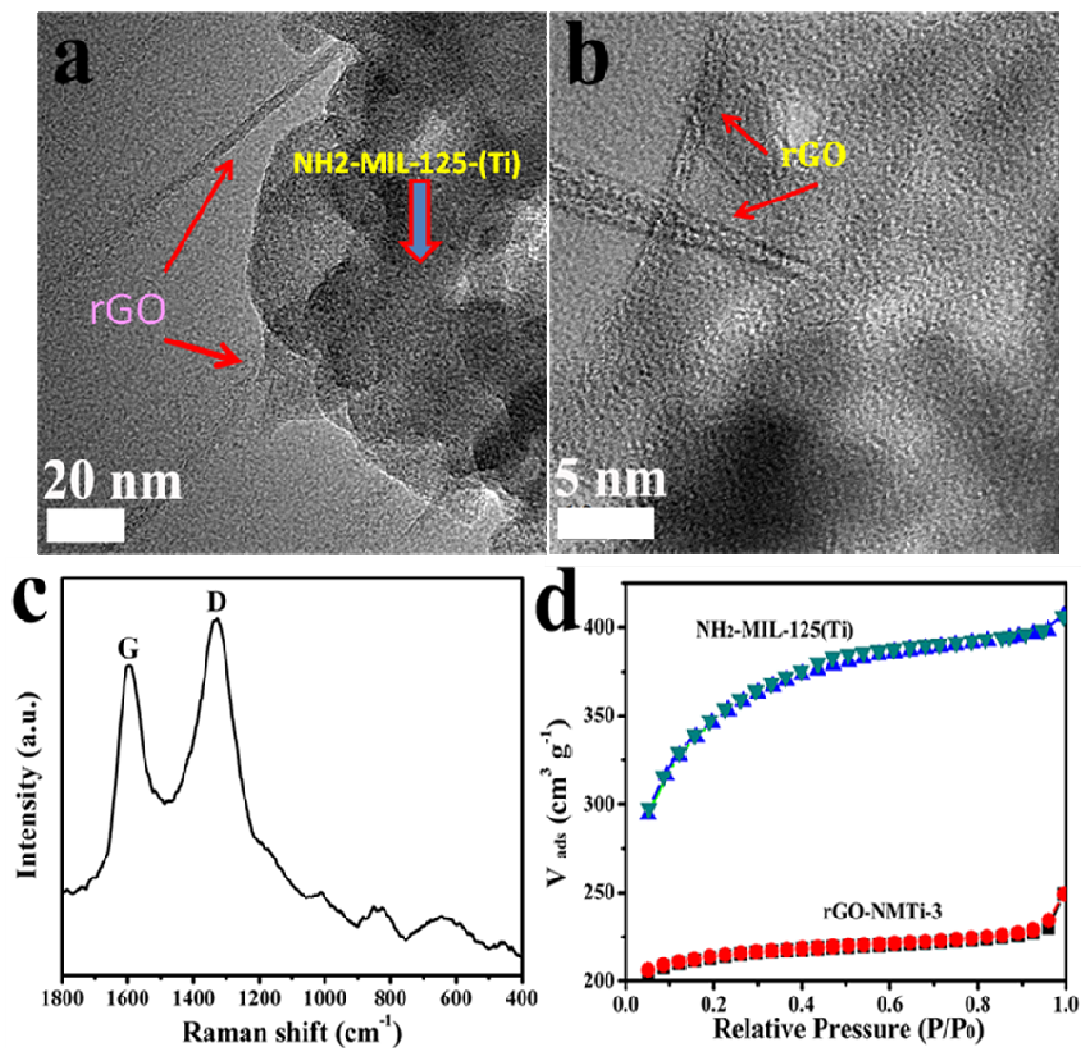
Fig. 5. (a, b) HRTEM images, (c) Raman spectra and (d) N_2 adsorption/desorption isotherms of rGO-NMTi-3 (or NH_2-MIL-125(Ti)).

Fig. 6. MO degradation photocatalytic performance of (a) no catalyst, (b) NH_2-MIL-125(Ti), (c) rGO-NMTi-1, (d) rGO-NMTi-2, (e) rGO-NMTi-3, and (f) rGO-NMTi-4.

Fig. 7. Schematic diagram showing the process of the photocatalytic dye degradation over the rGO-NMTi hybrid nanocomposite.

Fig. 8. (a) Recyclability, (b) HRTEM image, (c) XRD patterns and (d) Raman spectra of rGO-NMTi-3 photocatalyst in five successive cycles for degradation of MO under visible light irradiation.

Fig. 1. SEM images for the parent materials and the hybrid nanocomposites. (a) GO, (b) NH$_2$-MIL-125(Ti), (c) rGO-NMTi-1, (d) rGO-NMTi-2, (e) rGO-NMTi-3, and (f) rGO-NMTi-4.

Fig. 2. XRD patterns of (a) rGO, (b) NH$_2$-MIL-125(Ti), (c) rGO-NMTi-1,

(d) rGO-NMTi-2, (e) rGO-NMTi-3 and (f) rGO-NMTi-4 hybrid

composite.

Fig. 3. FT-IR spectra of (a) GO, (b) NH_2-MIL-125(Ti), (c) rGO-NMTi-1,

(d) rGO-NMTi-2, (e) rGO-NMTi-3, and (f) rGO-NMTi-4.

Fig. 4. UV–vis DRS spectrum of (a) rGO-NMTi-1, (b) rGO-NMTi-2, (c) rGO-NMTi-3, and (d) rGO-NMTi-4.

Fig. 5. (a, b) HRTEM images, (c) Raman spectra and (d) N_2 adsorption/desorption isotherms of rGO-NMTi-3 (or NH_2-MIL-125(Ti)).

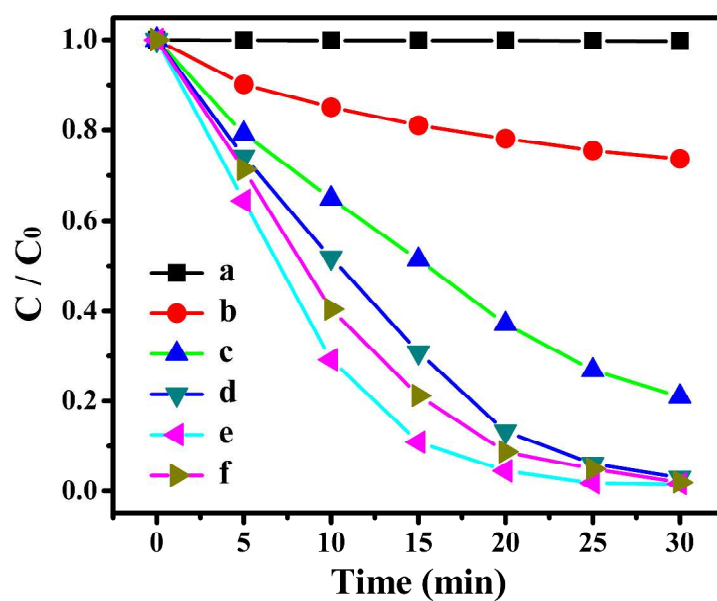**Fig. 6.** MO degradation photocatalytic performance of (a) no catalyst, (b) NH$_2$-MIL-125(Ti), (c) rGO-NMTi-1, (d) rGO-NMTi-2, (e) rGO-NMTi-3, and (f) rGO-NMTi-4.
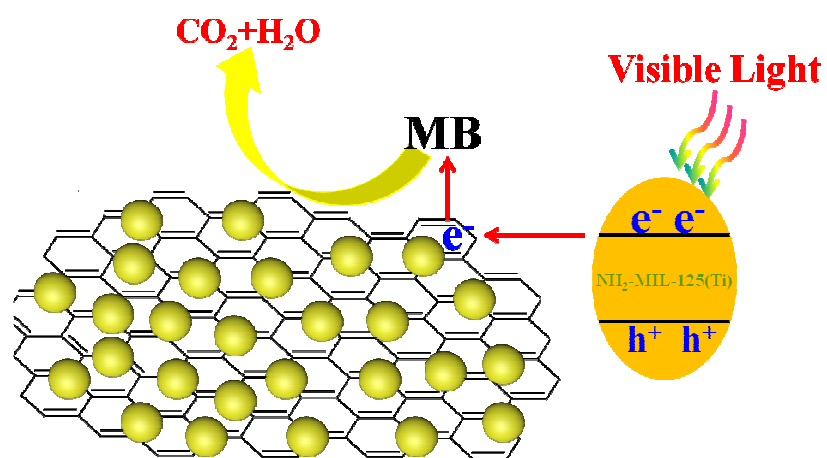
Fig. 7. Schematic diagram showing the process of the photocatalytic dye degradation over the rGO-NMTi hybrid nanocomposite.
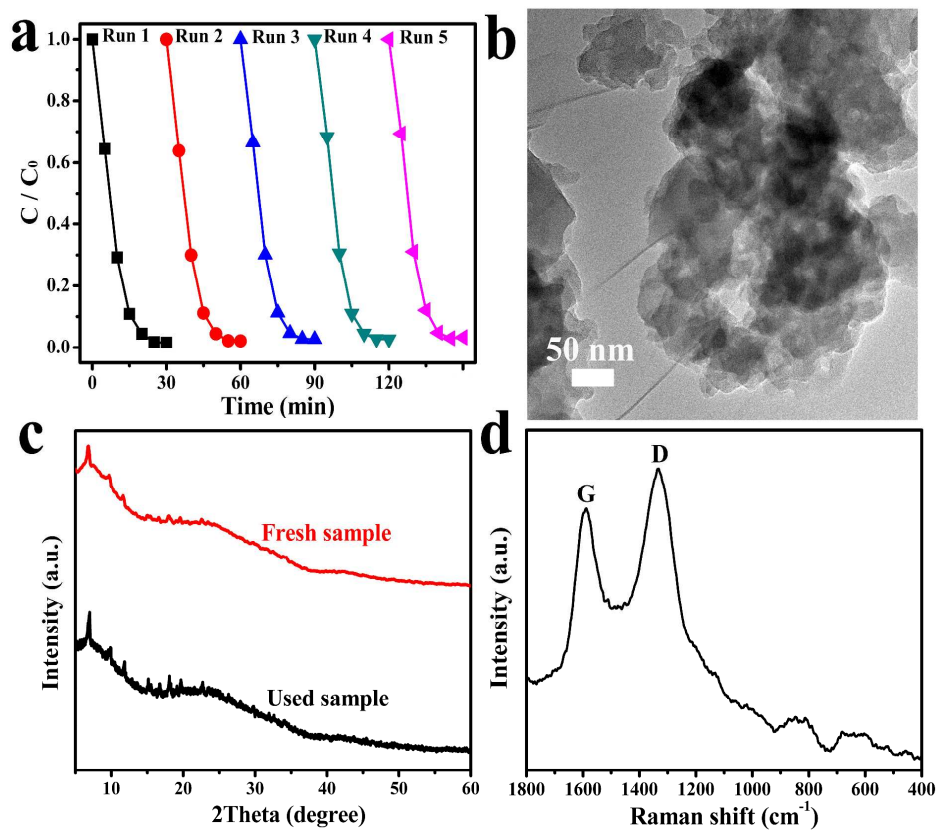
Fig. 8. (a) Recyclability, (b) HRTEM image, (c) XRD patterns and (d) Raman spectra of rGO-NMTi-3 photocatalyst in five successive cycles for degradation of MO under visible light irradiation.

CO_2+H_2O

Visible Light

MB

e^-

e^- e^-

NH_2-MIL-125(Ti)

h^+ h^+